IMPROVED CONSTITUTIVE DESCRIPTIONS OF THE FLOW BEHAVIOR OF AA2618

O.C. Obioha, J.D. Maile, U.P. Ochieze, C.H. Calhoun, M.H. Steiner, E.J. Payton *

Department of Mechanical and Materials Engineering, University of Cincinnati, 2851 Woodside Dr., Cincinnati, OH 45221 USA

Abstract

Aluminum alloy 2618 (AA2618) is a high-strength, heat-treatable alloy used widely in the aerospace and automotive sectors due to its excellent mechanical properties at elevated temperatures. The present research investigates hot working behavior of AA2618 through uniaxial compression from 300 to 500 °C and strain rates of 0.001 and 1 s^{-1}. Flow stress increases with strain rate and decreases with increasing temperature, as in similar alloys. However, strain hardening rates remain very low over three orders-of-magnitude of strain rate. Microstructural analyses suggest dynamic recrystallization occurs with secondary phase precipitates persisting through deformation and recrystallization. A constitutive model with temperature-dependent flow stress derived from the Lin-Wagoner model provided a substantial improvement over the Johnson-Cook and power law models.

Key words: *Aluminum alloy 2618; constitutive equation; stress-strain behavior; flow stress; microstructure*

1. Introduction

Aluminum alloy 2618 (AA2618) is a heat-treatable aluminum-copper-magnesium alloy that is often used in forged components for elevated-temperature applications, such as

Corresponding author. E-mail: paytonej@ucmail.uc.edu; Tel: 513-556-0260

engine pistons and compressor discs [1]. Strength at operating temperatures in the range of 300 to 500 °C is achieved through the presence of multiple intermetallic precipitates, including Al_2CuMg (S-phase) and Al_9FeNi [2]. The presence of precipitates at forming temperatures can lead to complex relationships between flow stress, strain, strain rate, and temperature during deformation.

Common constitutive relationships used for empirical modeling of flow stress during forging include the Johnson-Cook (JC) model, Holloman power-law, and Zener-Holloman Arrhenius-type equations [3]. These models often fail to adequately capture one or more aspects of the relationship between flow stress and forging conditions. Therefore, there is an ongoing need to develop constitutive models with a minimum number of parameters that are capable of more accurately capturing flow stress behavior in forming simulations. One approach often applied is the modification of these well-established constitutive relationships to incorporate parameters enabling more complex behavior to be represented [4].

Lin et al. [5] highlighted the ongoing need for constitutive model development in their investigation of compressive deformation of 2124-T851 aluminum (another alloy based on the Al-Cu-Mg system) over a wide range of temperatures and strain rates. They fitted a 5^{th} order polynomial to each adjustable parameter of a piecewise function composed of an Arrhenius-like constitutive law, the Zener–Hollomon relationship, and a hyperbolic function for different values of stress, activation, and strain hardening exponent. As pointed out by Wang et al, fitting of 4^{th} or 5^{th} order polynomials to accurately reflect the role of strain on parameters has been resorted to by numerous authors [4].

In another work, Wang et al. [4] proposed a newly modified Arrhenius constitutive form with a simplified functional structure to represent the flow stress behavior of 2219-O aluminum alloy. The model incorporated strain effects and was verified via finite element simulation of the compression process, showing lower prediction error than the classical Arrhenius law.

Parameterization of constitutive models has typically been done with a series of uniaxial stress-strain tests at different temperatures. In order to develop constitutive equations and analyze the flow behavior of Al 7050 alloys, the Gleeble thermomechanical simulator was used for experiments by Wu et al. [6] to calibrate the thermal activation, strain rate sensitivity, and dynamic softening during hot compression. The approximate values needed for the entire calibration of Al samples can be obtained from the Gleeble. Gleeble studies on aluminum alloy LY12 examined how heating rate affects the thermomechanical response, confirming that on-heating protocols are viable on aluminum and informative for constitutive calibration [7]. Constitutive equation validation with reduced numbers of specimens through non-isothermal or dynamically changing strain rate conditions is a potential use-case for Gleeble thermomechanical simulator testing, which has to date not been thoroughly explored.

The overall objective of this work is to provide a validated constitutive model that can be used in finite element simulations of hot forging or extrusion of AA2618 alloy, enabling accurate predictions of processing behavior. To address this objective, compression tests were performed at different strain rates and temperatures using the Gleeble thermomechanical simulator. The stress-strain behavior was fitted to different constitutive

models, and the flow behavior was rationalized through characterization of the microstructure after deformation.

2. Materials and Methods

The nominal chemical composition of AA2618 is presented in Table 1. Using the Pandat 2024 software (Computherm, LLC, Middleton, WI, USA) with the PanAl database, equilibrium phase fractions were calculated from the nominal composition and specification range for AA2618.

Table 1: Nominal chemical composition of AA2618 (wt.%)

Element	Cu	Mg	Fe	Ni	Ti	Si	Al
Composition	2.3	1.6	1.1	1.0	0.07	0.18	Balance
Composition range	1.9-2.7	1.3-1.8	0.9-1.3	0.9-1.2	0.04-0.1	0.1-0.25	Balance

Compression experiments at different temperatures and strain rates were carried out on a Gleeble 3500 thermomechanical tester (Dynamics Systems, Inc., Poestenkill, NY). Cylindrical specimens measuring 10 mm in diameter and 15 mm in length were extracted from the as-received material using electro-discharge machining.

Before testing, the specimens underwent thermocouple welding using a controlled voltage range of 20-40V, then graphite lubricant was applied to the contact surface between the specimens and the anvils to minimize frictional effects during deformation. The testing chamber was evacuated to create a vacuum environment (0.51 Torr),

effectively preventing oxidation of the specimens at elevated temperatures for the test duration. The specimens were compressed at temperatures of 300 °C, 350 °C, 400 °C, 425 °C, 450 °C, and 500 °C under controlled strain rates of 0.001 s^{-1} and 1 s^{-1}. Each specimen was held isothermally for 180 seconds before deformation to ensure thermal equilibrium throughout the material.

In addition to constant strain rate tests, strain-rate jump tests were conducted to further investigate the material's strain rate sensitivity. In this test, the specimens were initially deformed at 0.001 s^{-1} up to a true strain of 0.3, where the jump occurred. The crosshead speed was rapidly increased to impose a strain rate of 1 s^{-1} for the remainder of the compression test. During all tests, load and displacement data were recorded. These measurements were converted to true stress-true strain curves using standard correction procedures, accounting for machine compliance. Compliance corrections were applied following the approach of Sanchez-Avila et al. [8] to mitigate the influence of system deformation on the measured data.

Fitting of experimental behavior to various constitutive equations was performed by numerical optimization using the limited-memory Broyden-Fletcher-Goldfarb-Shanno algorithm with bound constraints (LBFGS-B) implemented within the minimize function in SciPy (v1.16.2). An objective function was formulated based on the weighted root-mean square error (RMSE) between the experimental data and the model-predicted data across all test conditions.

Experimental data were prepared using identical preprocessing steps as in the Johnson-Cook fitting approach. The stress-strain data were smoothed using a uniform filter, and down-sampled into pre-jump and post-jump segments to ensure balanced representation

across deformation stages. Specifically, higher weights were assigned to the pre-jump region due to the criticality of capturing the initial deformation behavior accurately, while moderate weights were used for the post-jump region.

After compression testing, the deformed AA2618 specimens were sectioned longitudinally to expose the mid-plane using a precision high speed saw fitted with an aluminum-oxide cut-off wheel operating at a cutting speed of 3000rpm. They were then mounted in epoxy to facilitate handling during grinding and polishing. The mounted samples were ground sequentially on SiC abrasive papers of 320, 400, 600, 800, and 1200 grit with continuous water flushing between each grinding step to prevent contamination from coarser grit being transferred to the finer abrasives. Polishing followed with diamond suspensions of 6 μm, 3 μm, and 1 μm, and a final polish using 0.05 μm colloidal silica to remove residual scratches and achieve the mirror-like finish required for accurate microstructural analysis. Grain boundaries and secondary phases were then revealed by chemical etching in Keller's reagent, which consists of 95% distilled water, 1.5% hydrochloric acid (HCl), 2.5% nitric acid (HNO_3), and 1% hydrofluoric acid (HF) with immersion for approximately 25 seconds, followed by a quick water rinse and drying. The etched longitudinal sections were examined by a 3D laser scanning confocal microscope (Keyence VK-X200 series, Itasca, IL, USA) at various magnifications to assess the microstructure. Grain size measurements for the as-received specimens were performed in accordance with the ASTM E112 standard using the Jeffries planimetric method. At least five random fields at 50X magnification were photographed, and grains were counted to determine the average grain size. The same preparation protocol was applied to the deformed specimens to enable direct comparison with the as-received condition.

3. Results

3.1 Initial Microstructure of AA2618

The initial microstructural examination revealed well-defined grain boundaries with equiaxed grains that are uniformly distributed, as shown in Figure 1. Additionally, several secondary phase particles, such as Al_9FeNi and Al_7Cu_4Ni, are visible as dark constituents, as shown in Figure 1. The measured grain sizes across five representative fields produced an average grain area of 345 μm^2, corresponding to an ASTM grain size of 9.54. Overall, the initial microstructure can be described as a recrystallized aluminum matrix with a fine equiaxed grains of a unimodal size distribution and a dispersion of hard intermetallic particles.

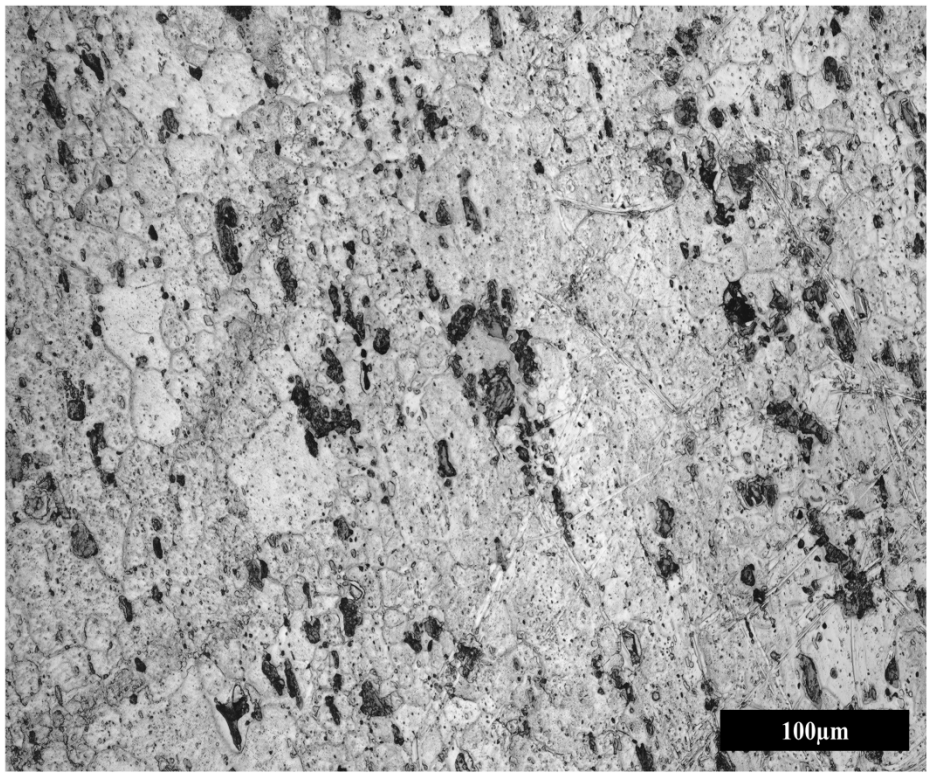

Figure 1: Representative optical micrograph of the as-received AA2618 alloy

Figure 2 shows the result of CALPHAD predictions. The alloy is only around 92% Face Centered Cubic (fcc) from the working temperature of 300 °C up to 660 °C, where liquid would be expected to start to form. Within the fcc phase are precipitates of various intermetallics/secondary phases, which consist of Al_3Ti, Al_7Cu_4Ni, Al_9FeNi, Mg_2Si, and $Ti_3Al_2Si_5$. The presence of such intermetallics is confirmed by the micrograph shown in Figure 1.

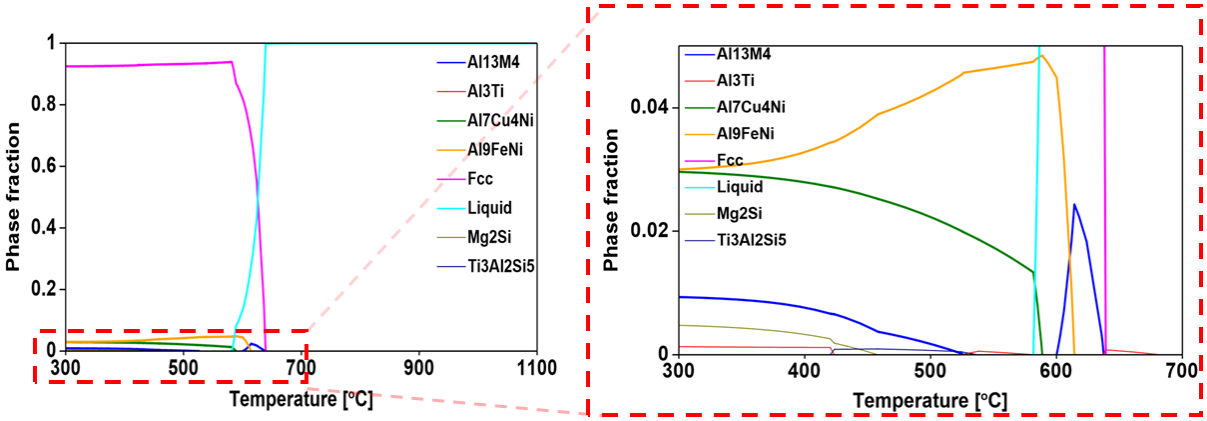

Figure 2: CALPHAD-predicted phase fraction of AA2618 as a function of temperature. The plot on the right magnifies the indicated region of the plot on the left

After compression was carried out, optical microscopy was performed on the deformed specimens across different temperatures and strain rate conditions. Figure 3(a-l) presents representative optical micrographs illustrating the deformed grain structures. The micrographs are grouped by strain rate condition across the working temperatures. Across all conditions, the micrographs show that the grains are slightly flattened in the loading direction and elongated in the longitudinal direction, consistent with an aspect ratio above unity. As shown in Figure 4a, AR values cluster around approximately 1.6-2.1, indicating that the post-deformation microstructure is not equiaxed and therefore likely not fully recrystallized at test conditions. Dispersed intermetallic precipitates remain evident throughout the matrix in all micrographs.

Figure 4b presents the grouped bar chart comparing mean ASTM grain size numbers for specimens deformed at four temperatures under three different strain rate conditions:

0.001 s^{-1}, 1.0 s^{-1}, and strain rate jump tests between these values. Each bar shows the mean ASTM grain size with standard error.

In general, a slight trend of grain refinement with increasing temperature is visible, with the ASTM grain size number increasing marginally at higher temperatures. The strain rate jumps condition shows comparable grain sizes to those observed in tests performed at equivalent final strain rates without jumps.

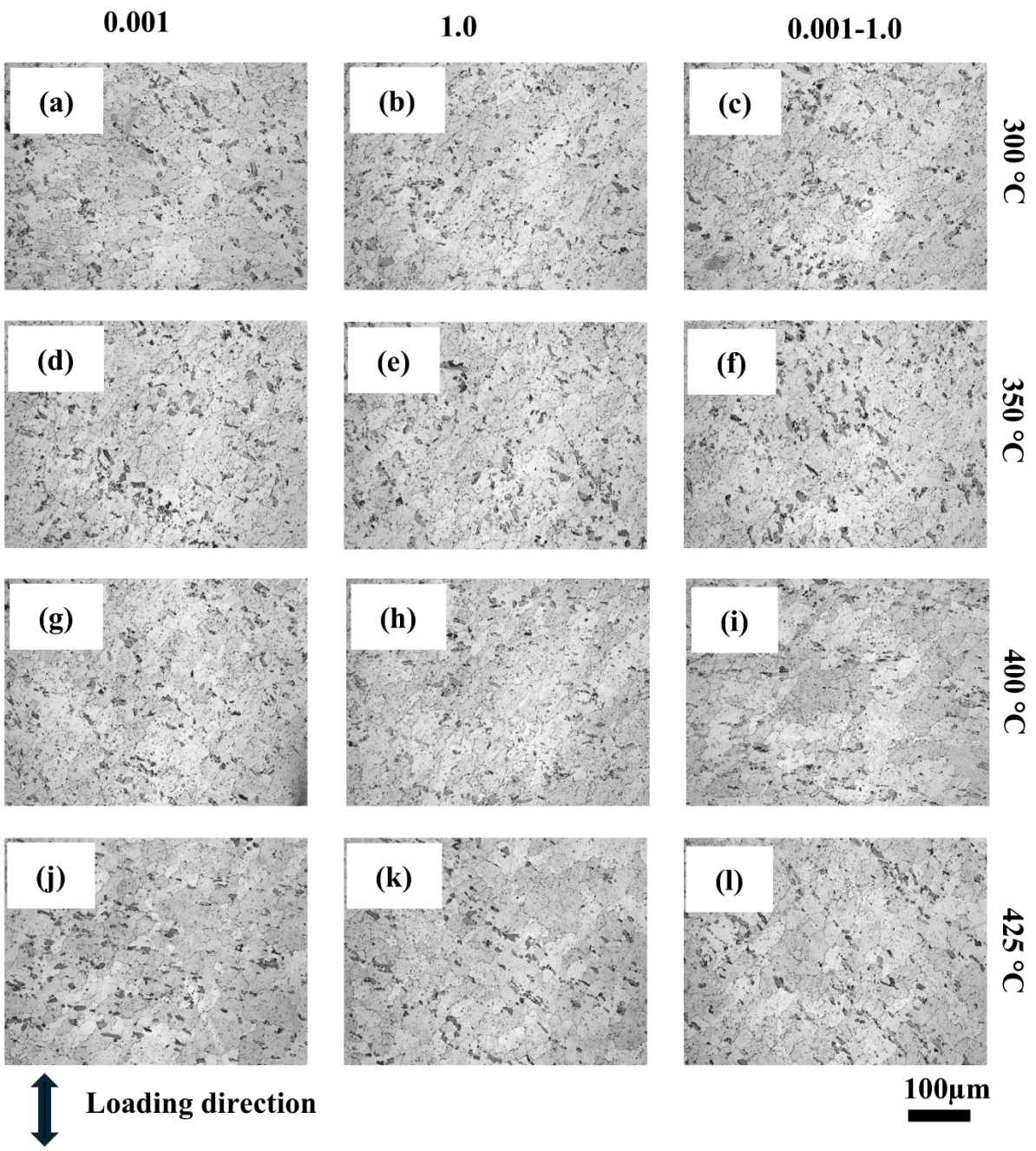

Figure 3: Representative optical microstructures of deformed specimens of the AA2618. (a-c) 300 °C, (d-f) 350 °C, (g-i) 400 °C, (j-l) 425 °C

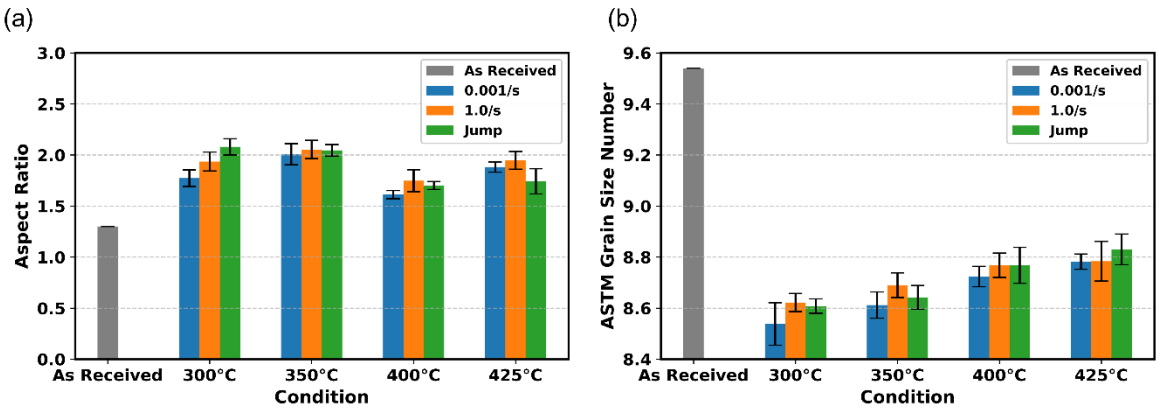

Figure 4: Microstructural metrics for AA2618 after uniaxial compression. (a) Mean grain aspect ratio and (b) mean ASTM grain size number for AA2618 specimens deformed at different temperatures and strain rates, with standard error bars

3.2 Phase analysis in AA2618

For each alloying element, Cu, Fe, Mg, Ni, Si, and Ti, a phase diagram was generated to show how varying the content affects phase constituency across temperatures. In each figure, the vertical red tie line indicates the nominal target composition of the element, while the blue vertical dotted lines indicate the range of interest within the plot as shown in Table 1. By tracing horizontally from each test temperature to the tie line, the specific phases predicted by CALPHAD can be identified. The volume fraction of different intermetallic phases are anticipated to affect the flow stress and slight composition variations may remain after homogenization and secondary processing. knowledge of possible variation in phases can be useful for interpreting differences in mechanical properties and microstructure evolution between melts of the same specification.

Figure 5a and 5b illustrate the effect of varying Cu and Fe content, respectively. At the nominal copper level, the tie line intersects the phase fields that include the FCC-Al and the intermetallic phases Al_7Cu_4Ni and Al_9FeNi. Tracing the tie line shows that at 300 °C, the phases present include $Al_{13}M_4$, Al_3Ti, Al_7Cu_4Ni, Al_9FeNi, FCC-Al, and Mg_2Si. This phase combination remains unchanged at 350 °C, showing that the intermetallics stay stable at intermediate forging temperatures. As the temperature rises to 400 °C, the tie line continues to pass through the same region, confirming the persistence of strengthening phases, particularly Al_7Cu_4Ni and Al_9FeNi. Even at a higher test temperature of 425 °C, the same phase field is stable with an inclusion of $Ti_3Al_2Si_5$. In Figure 5b, the tie line at the nominal Fe content indicates that at 300 °C, the stable phases include $Al_{13}M_4$, Al_3Ti, Al_7Cu_4Ni, Al_9FeNi, FCC-Al, and Mg_2Si. This combination remains the same at 350 °C, implying that iron stabilizes both the Fe-Ni-rich intermetallics and minor phases. At 400 °C, the tie line crosses into a region where $Ti_3Al_2Si_5$ emerges, and at 425 °C, the phase field remains the same.

For the Mg variation in Figure 5c, the tie line shows that at 300 °C, the predicted phases include $Al_{13}M_4$, Al_3Ti, Al_7Cu_4Ni, Al_9FeNi, FCC-Al, and Mg_2Si. This set remains stable at 350 °C. At 400 °C and 425 °C, there is a slight shift with Mg_2Si becoming less dominant as $Ti_3Al_2Si_5$ starts to appear alongside the FCC-Al matrix and other key intermetallics. Figure 5d depicts how varying Ni content influences phase stability. The tie line at the nominal Ni level confirms that at 300 °C and 350 °C, the FCC matrix coexists with $Al_{13}M_4$, Al_3Ti, Al_7Cu_4Ni, Al_9FeNi, and Mg_2Si. At 400 °C, the tie line shifts into a region where $Ti_3Al_2Si_5$ emerges alongside the existing phases. This phase combination persists up to 425 °C, where Mg_2Si loses stability.

For Si variation as shown in Figure 5e, the tie line shows that at 300 °C, the present phases are $Al_{13}M_4$, Al_3Ti, Al_7Cu_4Ni, Al_9FeNi, FCC-Al, and Mg_2Si. These compositions remain stable at 350 °C as well as 400 °C. When the temperature rises to 425 °C, the line enters a region where $Ti_3Al_2Si_5$ becomes significant, replacing Mg_2Si. In Figure 5f, it is shown that at the nominal Ti level, the tie line intersects a region containing $Al_{13}M_4$, Al_3Ti, Al_7Cu_4Ni, Al_9FeNi, FCC-Al, and Mg_2Si at 300 °C. This remains the same at other testing temperatures, 350 °C, 400 °C, and 425 °C. The dissolving and integration of Mg_2Si and $Ti_3Al_2Si_5$ start occurring at 450 °C.

Comparison of the subfigures of Figure 5 shows that there is a significant change in the compositions of intermetallic phases between 400 °C and 450°C. In some cases, such as Si and Mg, the phase constituents vary within the allowed specification range.

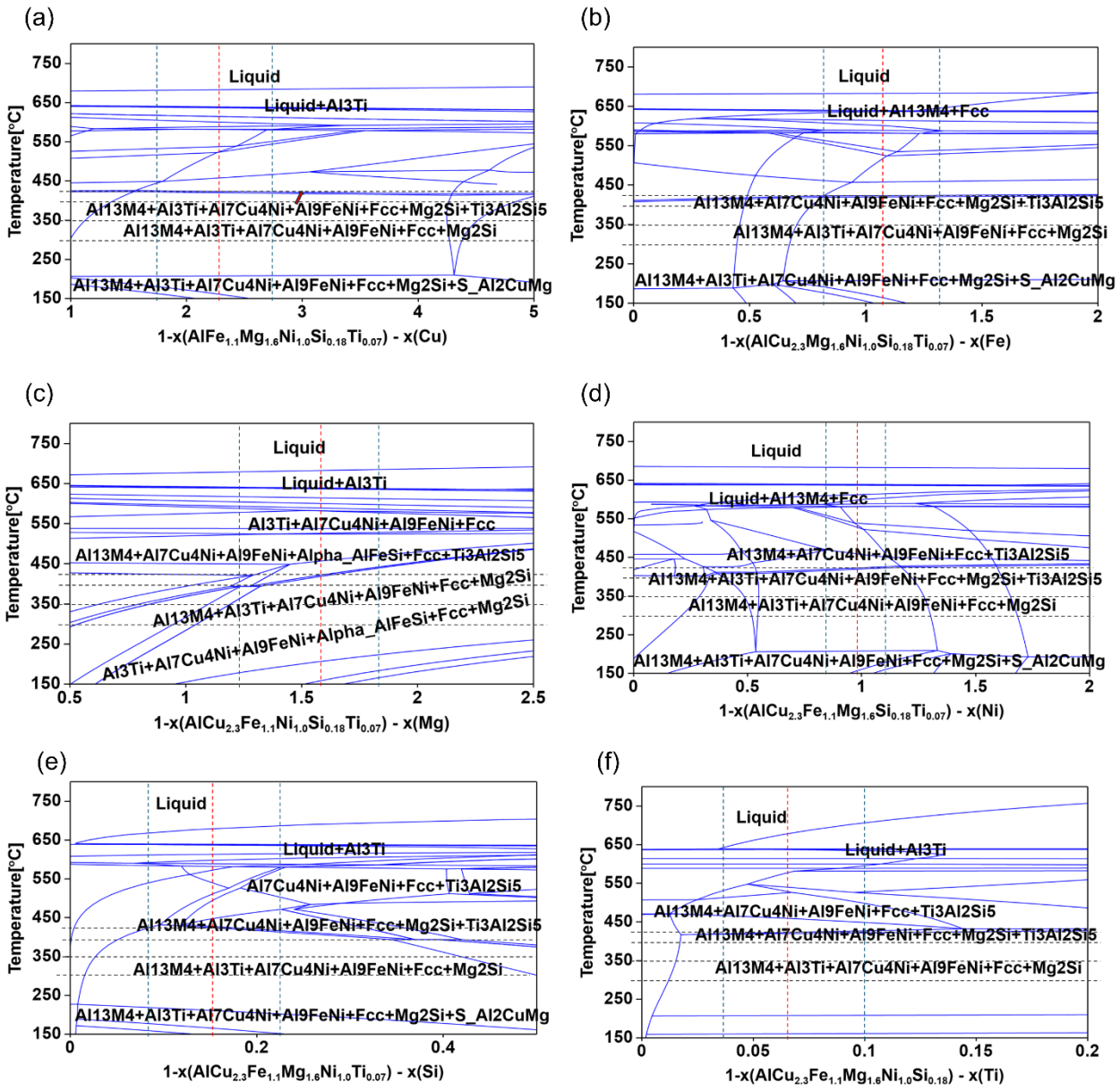

Figure 5: Psuedo Binary Phase diagram of AA2618 (a) 1-x($AlFe_{1.1}Mg_{1.6}Ni_{1.0}Si_{0.16}Ti_{0.07}$) – x(Cu), (b) 1-x($AlCu_{2.3}Mg_{1.6}Ni_{1.0}Si_{0.16}Ti_{0.07}$) – x(Fe), (c) 1-x($AlCu_{2.3}Fe_{1.1}Ni_{1.0}Si_{0.16}Ti_{0.07}$) – x(Mg), (d) 1-x($AlCu_{2.3}Fe_{1.1}Mg_{1.6}Si_{0.16}Ti_{0.07}$) – x(Ni), (e) 1-x($AlCu_{2.3}Fe_{1.1}Mg_{1.6}Ni_{1.0}Ti_{0.07}$) – x(Si), (f) 1-x($AlCu_{2.3}Fe_{1.1}Mg_{1.6}Ni_{1.0}Si_{0.16}$) – x(Ti)

3.3 Mechanical behavior

A series of stress-strain curves obtained from the hot compression testing of AA2618 at different deformation temperatures is shown in Figures 6 and 7. The plots generated are stress-strain curves at 1 s^{-1}, 0.001 s^{-1}, and strain jump curves, respectively. The results highlight the significant influence of temperature and strain rate on the flow stress of the alloy. At a strain rate of 1 s^{-1}, the flow stress is substantially higher than at lower rates. For example, in Figure 6a, at 1 s^{-1} and 300 °C, AA2618 reaches a peak true stress in the range of 145-160 MPa; at this peak, the flow remains relatively flat. As the temperature increases, the flow stress at 1 s^{-1} decreases notably: at 400 °C, the peak stress is around 80 MPa, and at 425 °C, it drops to approximately 70 MPa.

By contrast, at a strain rate of 0.001 s^{-1} (Figure 6b), the material shows softening and a lower overall flow stress. At 300 °C and 0.001 s^{-1}, the peak stress is about 60 MPa. When the deformation temperature is increased at the same slow strain rate, the flow stress decreases.

To further probe the material's strain rate sensitivity and to access fitting of constitutive equations using fewer test, a strain-rate jump test was carried out (Figure 7). In this test, the specimen was initially deformed at 0.001 s^{-1} up to 0.3 strain, and the rate was abruptly increased to 1 s^{-1}. The resulting stress-strain curve (Figure 7) shows a distinct response at the moment of the rate change; when the strain rate is increased, the flow stress immediately rises due to the material's strain rate sensitivity. For example, just before the

jump at 0.001 s^{-1} up to 0.3 strain, the stress level was approximately 65 MPa at 300 °C; immediately after switching to 1 s^{-1}, the stress spiked to approximately 145 MPa.

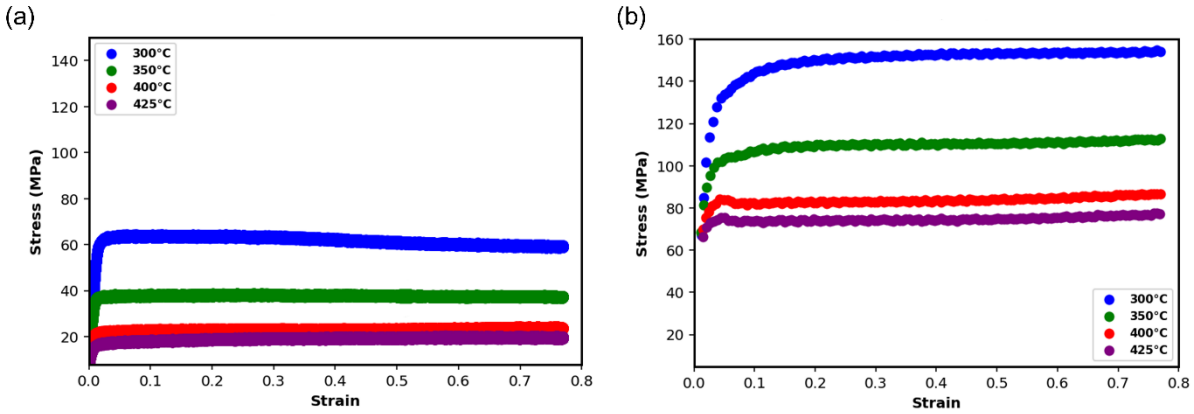

Figure 6: True stress-strain curve of AA2618 at (a) 1 s^{-1} and (b) 0.001 s^{-1} for temperatures 300 ˚C to 425 ˚C.

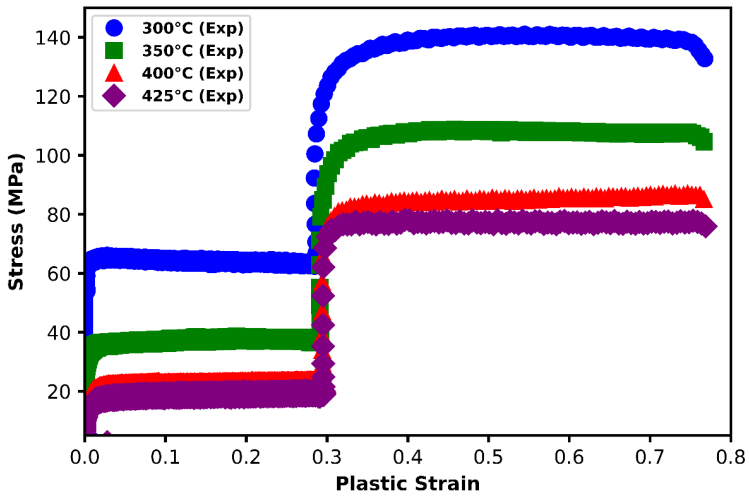

Figure 7: True stress-strain curve for the strain jump test. The material is initially deformed at 0.001 s^{-1} (up to ε = 0.3), then the strain rate is increased to 1 s^{-1}.

3.4 Constitutive Models Formulation and Parameter Identification

To accurately model the behavior of AA2618 during forging, a calibrated constitutive model is needed. Several constitutive models, such as the power law and Johnson-Cook equations, are commonly used to capture different aspects of how stress evolves with changes in strain, strain rate, and temperature during deformation.

3.4.1 Power law

The power law model provides a good starting approach for describing the relationship between flow stress, strain, and strain rate. The model assumes a direct dependency of the flow stress on strain raised to the work hardening exponent and strain rate raised to the strain rate sensitivity exponent.

$$\sigma = A\varepsilon^{n}\dot{\varepsilon}^{m} \tag{1}$$

In which σ is the flow stress (MPa), $\dot{\varepsilon}$ is the strain rate, n is the work hardening exponent, m is the strain rate sensitivity, ε is the strain and A is a material constant.

The power law was initially fitted to the experimental true stress-strain data for each deformation temperature. The fitting showed good alignment in describing the general flow curve shape for steady-state conditions. However, the power law model is limited in accurately representing the changes that occur during a strain rate jump, as seen in this work. This is because it does not effectively separate strain rate and temperature effects very well to handle these quick transitions.

Figure 8: Comparison of experimental and power law model fitted stress-strain curves for AA2618 alloy subjected to strain-rate jump tests. (a) Best fit parameters allowing A to vary with temperature. (b) The relationship between A and T.

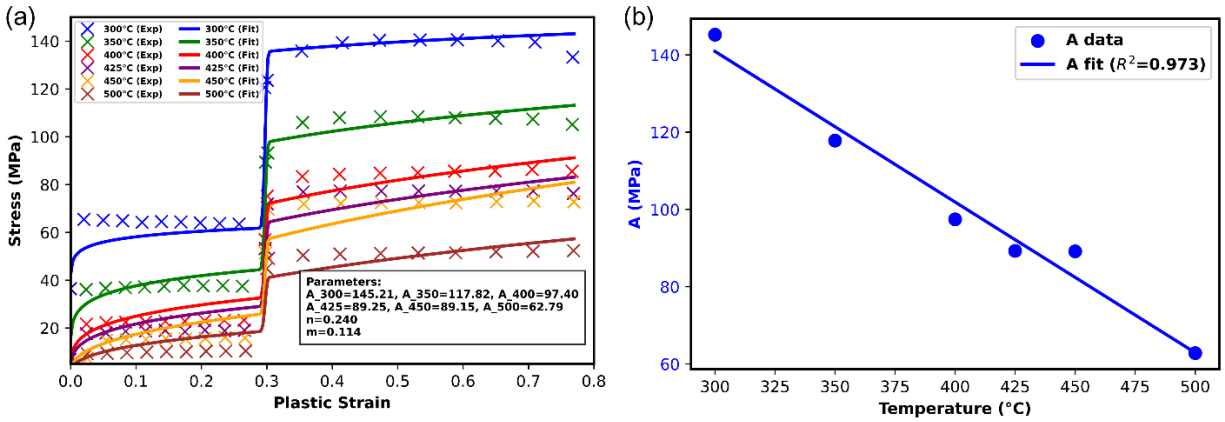

3.4.2 Johnson-Cook (JC) model

The phenomenological Johnson-Cook (JC) constitutive model [9] considers the effects of strain hardening, strain rate, and thermal softening, and is expressed as:

$$\sigma = \left[A + B\ \varepsilon_p^n\right]\left[1 + C\ ln\left(\frac{\dot{\varepsilon}}{\dot{\varepsilon}_0}\right)\right]\left[1 - \left(\frac{T}{T_m}\right)^m\right] \quad (2)$$

where σ is flow stress, ε_p^n is the equivalent plastic strain (MPa), $\dot{\varepsilon}$ is the strain rate, and $\frac{T}{T_m}$ is the temperature term. In this formulation, A is the yield strength at the reference condition, B and n describe strain hardening behavior, C is the strain rate sensitivity coefficient, $\dot{\varepsilon}_0$ as the reference strain rate taken at 1 s^{-1}, and the parameter m controls the thermal softening effect.

The five JC parameters (A, B, n, C, and m) were determined by fitting the model to the measured stress-plastic strain curves where the fitted parameter A decreases sharply

with temperature while the rate sensitivity coefficient C increases, which together captures thermal softening. Also, the work hardening exponent n is small, so the post-yield segments are nearly horizontal which is consistent with the material near-perfect plastic response. The results of this fitting are shown in Figure 9.

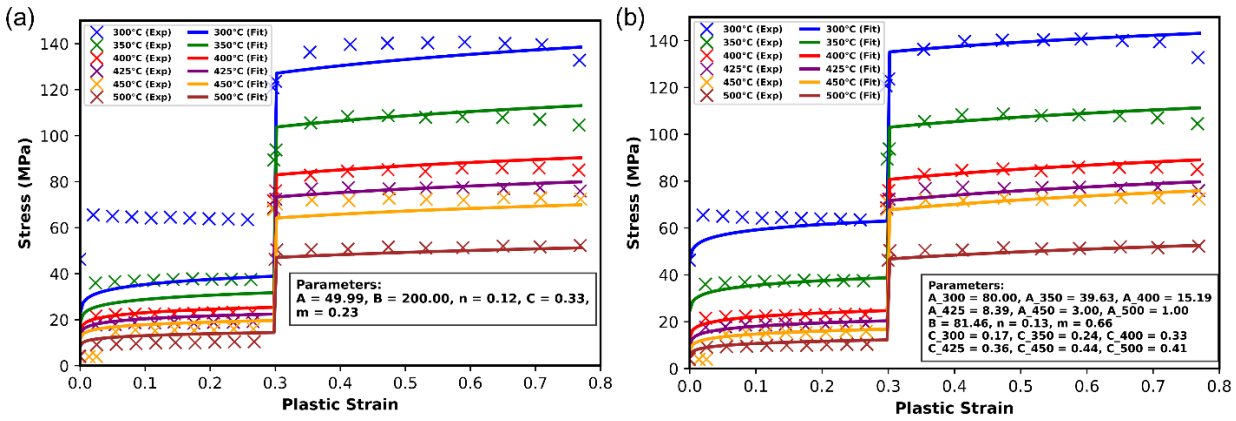

Figure 9: Comparison of experimental and Johnson-Cook model fitted stress-strain curves for AA2618 alloy subjected to strain-rate jump tests. (a) Constant values of A, B, n, C, m; (b) Best fits for each temperature allowing A and C to vary with temperature. Values for the parameters A and C corresponding to (b) are shown in Figure 11.

3.4.3 Lin- Wagoner model

The Lin-Wagoner constitutive model is mathematically expressed as [10]:

$$\sigma = A\{1 - Bexp\big(C_1 + C_2(T - T_0)\big)\varepsilon\}\left(\frac{\dot{\varepsilon}}{\dot{\varepsilon}_0}\right)^m \left(\frac{T}{T_0}\right)^\beta \qquad (3)$$

where σ is the flow stress (MPa), A , B , C_1 , C_2 are material constant, ε is plastic strain, $\dot{\varepsilon}$ and $\dot{\varepsilon}_0$ are the applied and reference strain rates, respectively. T and T_0 represent the forming temperature and reference temperature (298 K), respectively. The parameter m is the strain rate sensitivity exponent and β is the thermal sensitivity exponent. Parameter A was optimized independently for each temperature, while the remaining parameters were fitted globally across all conditions. As shown in Figure 10a, this captured the post-jump plateaus but left a noticeable misalignment in the pre-jump region, indicating that the overall strength scale varies systematically with temperature beyond what the baseline form permits.

To address this, A was allowed to vary with temperature, replacing A with $A(T)$ while keeping the other parameters global. The modification is expressed as

$$\sigma = A_T \{1 - Bexp\big(C_1 + C_2(T - T_0)\big)\varepsilon\} \left(\frac{\dot{\varepsilon}}{\dot{\varepsilon}_0}\right)^m \left(\frac{T}{T_0}\right)^\beta \qquad (4)$$

In practice, one value of A was estimated independently at each test temperature hence the notation A_T. This single modification removed the pre/post-jump mismatch and produced good agreement across the full dataset as seen in Figure 10b, confirming that a temperature dependent A is the principal adjustment required by the data. The per-temperature A values were then regressed against temperature to obtain a linear temperature dependence,

$$A(T) = A_0 + A_1 T \qquad (5)$$

Substituting this into the Lin- Wagoner model gives

$$\sigma = (A_0 + A_1 T) \{1 - B\exp\big(C_1 + C_2(T - T_0)\big)\varepsilon\} \left(\frac{\dot{\varepsilon}}{\dot{\varepsilon}_0}\right)^m \left(\frac{T}{T_0}\right)^\beta \qquad (6)$$

With A_0 and $A_1 T$ fixed by the A versus T regression, only B , C_1 , C_2, m, and β were fit globally. Figure 10c shows that this linear $A(T)$ preserves the quality of fit while reducing the numbers of free parameters. Finally, motivated by the horizontal stress-strain response after yielding, the strain dependent term in braces was removed to test a strain neutral variant:

$$\sigma = A(T)\left(\frac{\dot{\varepsilon}}{\dot{\varepsilon}_0}\right)^m \left(\frac{T}{T_0}\right)^\beta \tag{7}$$

where $A(T) = A_0 + A_1 T$

As illustrated in Figure 10d, this simplified form still reproduces the measured pre and post-jump stress levels indicating that, under the present conditions, the response is dominated by a temperature indexed strength scale and rate sensitivity, with negligible work hardening consistent with the observed near-perfectly-plastic behavior.

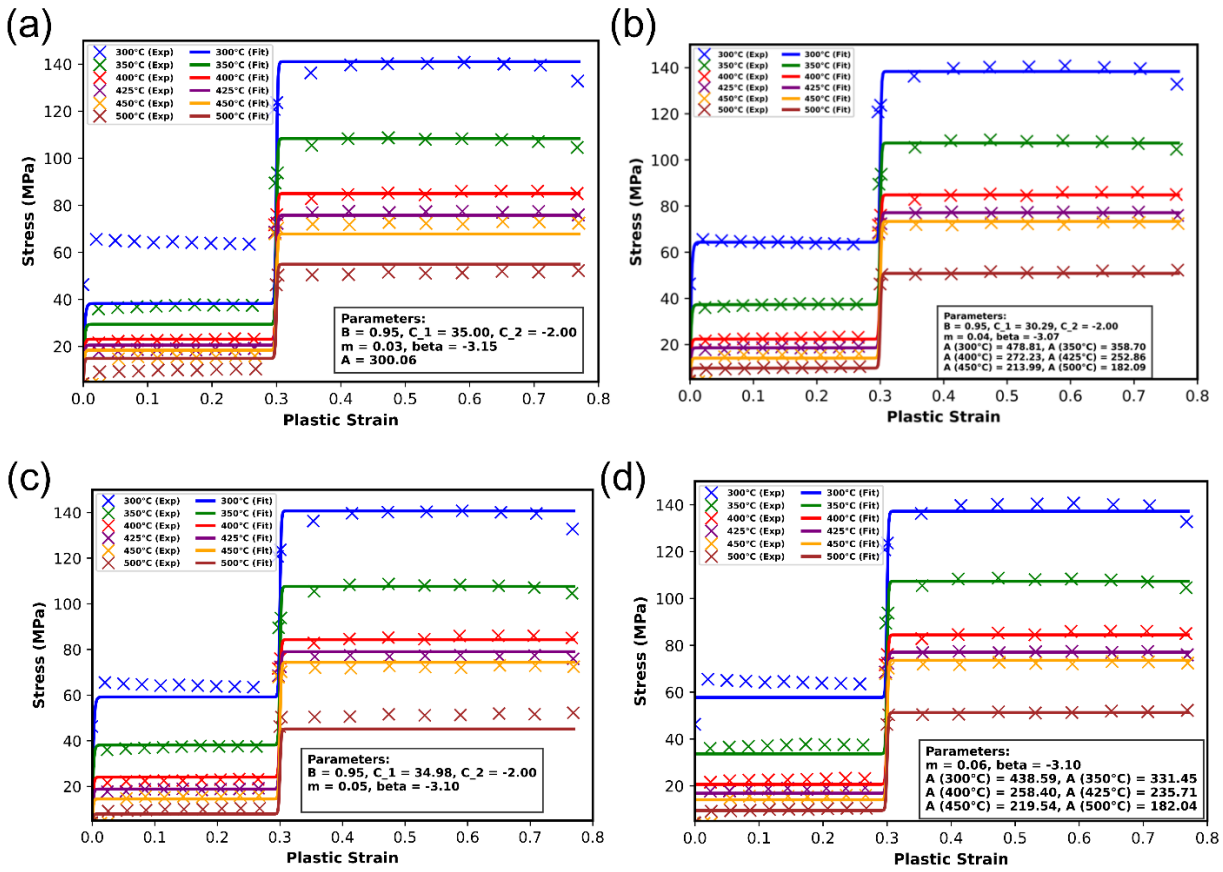

Figure 10: Progressive calibration of the Lin-Wagoner model for AA2618 strain rate jump test (a) Original LW, (b) Fitting $A(T)$at each temperature, (c) Linear form with $A(T)$, (d) Strain neutral variant

3.5 Temperature-dependent parameter A and its trends

In both constitutive descriptions, the parameter A is treated as a function of temperature, $A(T)$. In the Johnson-Cook model, A represents the reference strength at the baseline strain and strain rate, allowing A to vary with temperature captures the thermal softening.

The Johnson-Cook rate sensitivity coefficient was likewise modeled as temperature-indexed, $C(T)$ reflecting the observed increase in rate sensitivity at higher temperatures. The A-temperature plots, as shown in Figure 11 for both models, show a monotonic decrease of A with increasing T, consistent with thermal softening (the largest A at 300 ˚C, smallest at 500 ˚C). In the Johnson-Cook result, where $A(T)$ and $C(T)$ are shown together, C increases with temperature, indicating stronger rate sensitivity at elevated temperatures.

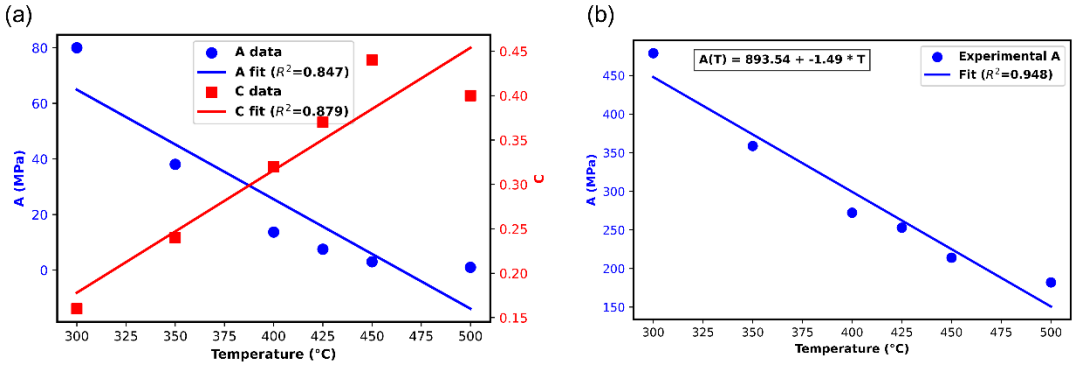

Figure 11: Temperature-indexed parameters versus temperature for (a) Johnson-Cook (b) Lin-Wagoner models

3.6 Post-deformation analysis

To further probe why AA2618 tends toward a near perfect-plastic response after yielding and why the grain size varies so little over the temperature and strain rate ranges investigated, we quantified the volume fraction and circle-equivalent diameter of second-phase intermetallics observed in the micrographs for each condition. These phases will

exert a pinning pressure on grain boundaries, limiting the grain size to a value D proportional to $\frac{2d}{3f}$ where d is the diameter of the particles and f is their volume fraction. A scatter plot of $\bar{l}$ vs D, is shown in Figure 12, with points in color groupings according to test temperature. While there is some observed clustering with respect to temperature, no strong correlation is observed to exist between the measured grain size and the Zener limiting grain size, and the ranges of variation are very small in both cases.

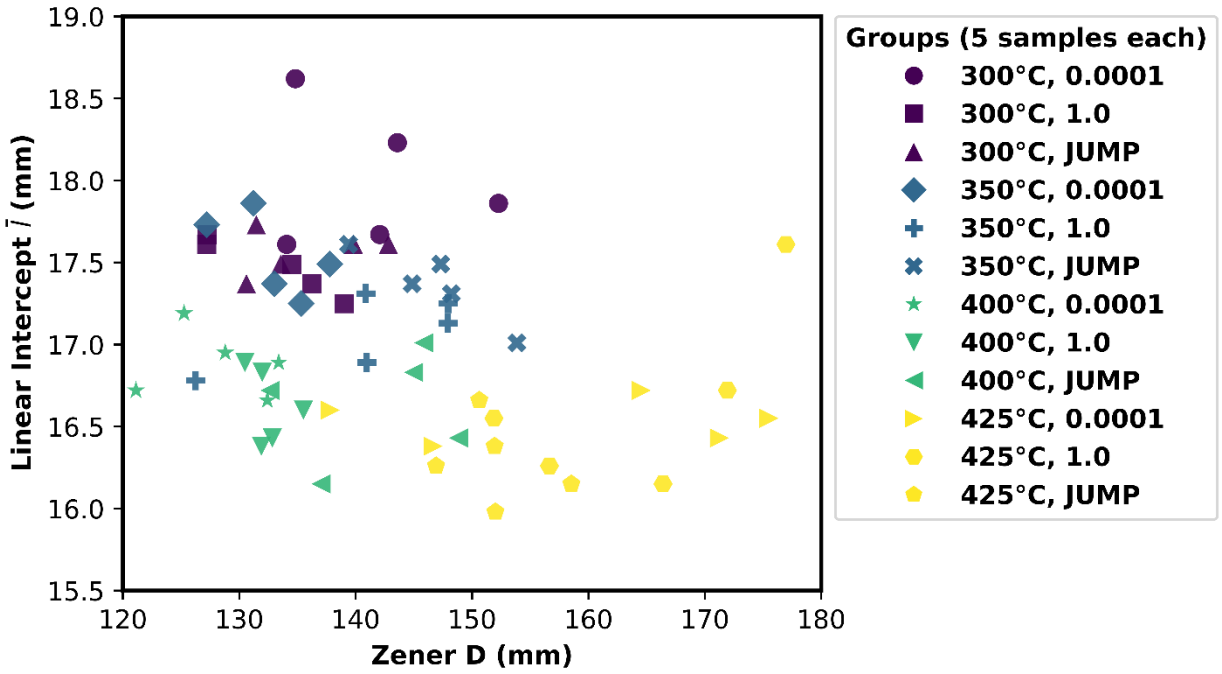

Figure 12: Scatter plot of experimentally observed grain size (characterized by mean lineal intercept length) against the Zener limiting grain size (calculated from the measured mean size and volume fraction of precipitates)

4. Discussion

4.1 Microstructure evolution and grain structure

The as-received microstructure contains fine equiaxed grains averaging approximately 345 μm^2 corresponding to an ASTM grain size number of 9.54. Post-deformation microstructural analysis, as shown in Figure 3, reveals that the grains were elongated and flattened perpendicular to the compression axis. This is consistent with dislocation slip-dominated plasticity, with an incomplete dynamic recrystallization (DRX). The nearly perfectly-plastic behavior with virtually no strain hardening (cf. Figs 6 & 7) further supports the conclusion that recrystallization is not widespread in this alloy during compression in the range of 300-500 °C, since some strain hardening would be expected to accompany the increase in stored strain energy from dislocation accumulation that recrystallization relieves. Rather, the stress-strain curves and the microstructure both point toward a substantial amount of dynamic recovery occurring, limiting strain hardening and resulting in incomplete continuous dynamic recrystallization.

The slight increase in ASTM grain size number shown in Figure 4b for all deformed conditions indicates that a limited amount of dynamic recrystallization probably does occur. Interestingly, deformation at higher temperatures results in a finer grain size, as shown in Figure 4b. This suggests deformation at the higher temperatures might increase nucleation site density, leading to the formation of more new strain-free grains than at lower temperatures. Such a change in microstructure is counterintuitive because dislocation climb kinetics and grain coarsening kinetics both follow Arrhenius relationships with temperature. Thus, it would usually be anticipated that fewer grains would be observed per unit area due to grain growth during deformation in which dynamic

recrystallization is not occurring. Likewise, it would be anticipated that less dislocation accumulation would occur at the higher temperatures due to dynamic recovery, therefore reducing the driving force for recrystallization. It is clear from Figure 4 that the behavior of AA 2618 in this temperature range contradicts both of those conventional explanations. A plausible possible explanation for the reduction in grain size at higher deformation temperatures could be due to accelerating the recovery of the relatively small amount of dislocation accumulation into subgrain cell walls.

The same intermetallic particles responsible for maintaining the alloy's high-temperature strength are also often found to be contributors towards precipitation hardening and dislocation pinning [11]. This alloy contains multiple intermetallic phases, such as Al_2CuMg and Al_9FeNi (as indicated in the phase diagrams predicted by CALPHAD in Figure 5) that are stable over the examined temperature range. As noted elsewhere (e.g. Huang et al. [12]), these secondary phases can act as pinning agents, limiting the mean free paths of dislocations, promoting dynamic recrystallization, promoting grain boundary sliding, and hindering grain boundary migration. The low hardening rate and increased aspect ratios after deformation suggest the secondary phases in this alloy do not play a key role in dislocation density-driven microstructure evolution in this temperature range. While high strain rate sensitivity is often an indicator of grain boundary sliding as a strain accommodation mechanism, grain boundary sliding typically results in a more equiaxed grain structure after deformation.

The secondary phases appear to play an important role in limiting grain growth during the deformation process, which is why clustering is observed in Figure 12 and also why the ranges of values for both D and $\bar{l}$ in Figure 12 are small. Despite the high homologous

temperature, the grain size remains relatively stable, likely due to the Zener pinning pressure exerted on the grain boundaries by the secondary phases. This appears contradictory to, for example, the findings of Kaibyshev et al. [13], who noted that aluminum alloys predominantly undergo dynamic recrystallization at high temperatures, where subgrains gradually transform into high-angle boundaries. A significant change in the deformation mechanism with temperature would be expected to be reflected in the microstructure and its evolution.

To further assess the degree to which DRX occurred, consider the scenario depicted schematically in Figure 13. Assuming an initially equiaxed grain represented as a sphere, this grain should deform into an oblate spheroid with the same volume as the initial sphere if the grain is deformed unconstrained. In the present work, the cylinders in the Gleeble experiments started out with a length of 15 mm and were compressed to a 7 mm final length. The macroscopic engineering strain for the specimen is given by $\epsilon_e = \frac{\Delta l}{l_0} = \frac{7-15}{15} = -0.53$. This is converted to true strain as $\epsilon_t = \ln(\epsilon_e + 1) = -0.76$. For an incompressible material, the sum of the strains in all principal directions must be zero: $\epsilon_x + \epsilon_y + \epsilon_z = 0$. In the case of an infinitely rotationally symmetric object, like a sphere or oblate spheroid, $\epsilon_x = \epsilon_y$. If the average grain in our material is compressed to $\epsilon_z = -0.76$, then we might expect $\epsilon_x \approx -\epsilon_z/2$, or 0.38.

We found a grain size in our initial condition of ASTM 9.54. Approximating an equiaxed grain as a sphere, this amounts an equivalent diameter of ~13 μm. After deformation in which no recrystallization occurred to alter the grain size, we might approximate the shape of an initially spherical grain as an oblate spheroid. Under this approximation, the

minor axis b of the oblate spheroid from the strain in the z direction would be $\sim 6.5\exp(-0.76) = 3.04\ \mu m$. The major axis length of the spheroid can be obtained using the relationship to the true strain in the x direction, $\epsilon_x = \int_{l_0}^{l_f} \frac{dl}{l} = \ln\left(\frac{l_f}{l_0}\right)$, where l_0 is given by the initial sphere diameter and l_f would be the major axis length a after deformation. Rearranging the equation, we obtain $a = l_f = l_0\exp(\epsilon_x) = 13\exp(0.38) = 9.05\ \mu m$.

For a measured aspect ratio of the grains in the x vs the z directions, $\alpha_{xz} = \frac{\bar{l}_x}{\bar{l}_z} = \frac{a}{b}$, the assumption of constant volume spherical grains results in an equation for $b = \left(\frac{3V}{4\pi\alpha_{xz}^2}\right)^{\frac{1}{3}}$ and $a = \alpha_{xz}b$. Taking an initial volume equal to that of the sphere of $13\mu m$ equivalent diameter (or, equivalently, the oblate spheroid with $a = 9.05\ \mu m$ and $b = 3.04\ \mu m$), the cross-sections of the hypothetical average grains with no recrystallization are compared to approximately spheroidal grains with the measured aspect ratios from the present work are compared in Figure 13.

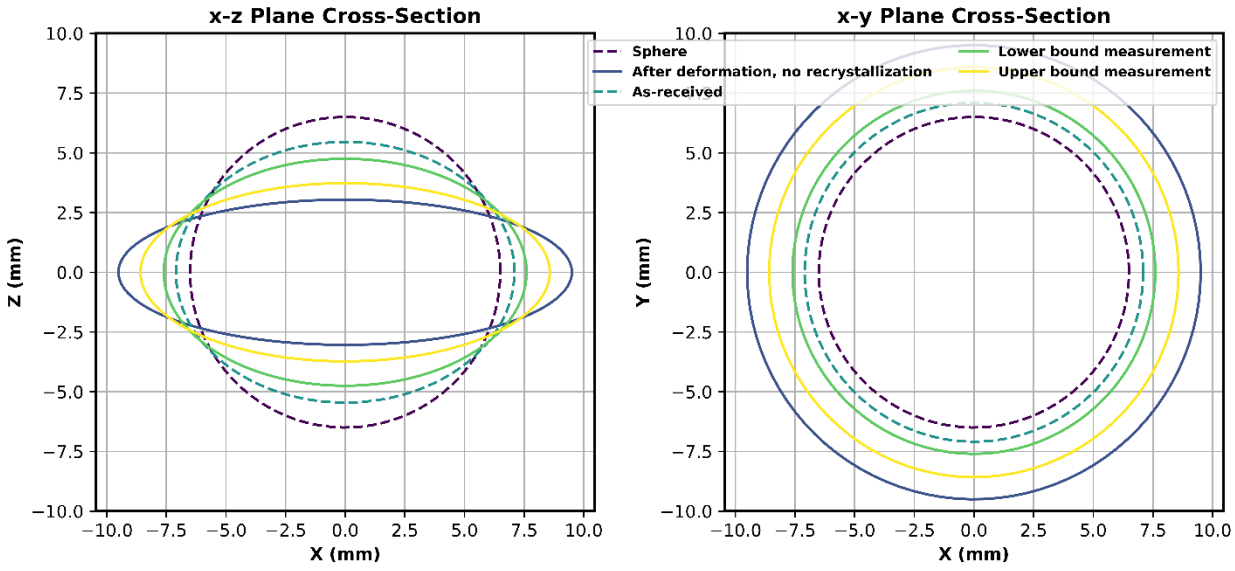

Figure 13: Schematic or geometric interpretation of grain aspect ratio after compression, comparing measured aspect ratios to the deformation of a spherical grain with no recrystallization. (a) View along transverse direction, with compression direction vertical; (b) View down compression direction axis.

It can be seen through comparison of the cases featured in Figure 13 that our measured aspect ratios fall between the ellipse resulting from purely plastic flattening and a circular cross-section representing a model of pure dynamic recrystallization. Across temperatures and strain rate conditions, the measured α_{xz} remains >1 and consistently below the no-recrystallization bound ($\alpha_{xz} = 3.13$), with values clustering around 1.6-2.1. This intermediate state indicates partial shape restoration attributable to incomplete recrystallization of the grain population within the available time-temperature-strain window. A slight decrease in α_{xz} with increasing temperature is consistent with thermally assisted recovery. However, α_{xz} > 1 at all conditions shows that grains do not revert to equiaxed morphologies.

Taking the equiaxed and no-recrystallization bounds as limiting cases, a linear mixture model of the aspect ratios estimates that perhaps between 30% and 60% of the grains in our microstructure at the end of deformation are recrystallized. This wide range is to be expected given (1) the likely dynamic nature of recrystallization at these temperatures, (2) the crude approximations involved in the estimate, and (3) the as-received material aspect ratio already exceeded unity.

4.2 Mechanical response and deformation mechanisms

In general, an increase in strain rate at a constant temperature is expected to result in higher flow stress, whereas an increase in deformation temperature at a given strain rate typically will typically lead to a reduction in flow stress [14],[15]. The present work is consistent with those expectations. For example, at a strain rate of 0.001 s^{-1}, the maximum flow stress was approximately 65 MPa at 300 °C and dropped to around 20 MPa at 425 °C. However, when the strain rate was increased to 1.0 s^{-1}, the flow stress rose significantly to about 155 MPa at 300 °C and approximately 65 MPa at 425 °C. These findings align with the observations reported by Mirzadeh, who emphasized the inverse relationship between temperature and flow stress and strain rate sensitivity of hot-deforming aluminum alloys [14].

Similarly, in the study on AA1050 reported by Yang et al [16], the flow curve is described as the outcome of a competition between work hardening and dynamic softening by dynamic recovery and continuous dynamic recrystallization, transitioning into a perfectly plastic regime for certain ranges of temperature and strain rate. They located the onset of dynamic recrystallization using the well-established critical strain criterion with ε_c proportional to the peak strain within the same temperature rate window [17]. The post-yield stress observed in the present work is essentially flat from 300 to 500 °C at both constant strain rates and in the strain rate jump tests, indicating that softening quickly offsets any incremental work hardening. Thus, our observations are clearly past the critical strain and within the recovery-dominated regime. Also, our work clearly demonstrates that the constitutive fits require an additional temperature dependence parameter and show a monotonic increase in rate sensitivity with temperature, mirroring

the trends reported for AA1050 by Yang et al. and consistent with classic interpretations of dynamic recovery controlled flow.

4.3 Constitutive modeling and predictive accuracy

The present work found that the JC model exhibits limitations in inaccurately capturing the stress transitions during strain-rate jumps, often underpredicting prejump stress levels. This aligns with Sung et al. [10] who emphasized the need for constitutive models to consider the combined effects of strain and temperature for high-strength aluminum alloys. Our modified LW model demonstrated significantly improved predictive accuracy, better representing temperature-dependence and material response to abrupt strain rate changes (cf. Figure 10). To quantify these models' differences, we evaluated goodness-of-fit using the coefficient of determination (R^2) for every temperature, as shown in Table 2.

Table 2: Coefficient of determination (R^2) for power law, Johnson-Cook and modified Lin-Wagoner fits across temperature (300-500 °C)

Temperature/model	**300 °C**	**350 °C**	**400 °C**	**425 °C**	**450 °C**	**500 °C**
Power law (Fig 8)	0.8434	0.8249	0.7483	0.7258	0.629	0.646
Original Johnson-Cook (Fig 9a)	0.563	0.860	0.895	0.884	0.846	0.862
Modified Johnson-Cook (Fig 9b)	0.860	0.893	0.896	0.876	0.855	0.865
Original Lin-Wagoner (constant A) (Fig 10a)	0.580	0.643	0.900	0.889	0.831	0.733

Lin-Wagoner (A independently fit for each T) (Fig 10b)	0.852	0.938	0.896	0.883	0.871	0.952
Modified Lin-Wagoner (linear $A(T)$) (Fig 10c)	0.7362	0.9473	0.8289	0.8545	0.843	0.6011
Modified Lin-Wagoner- (no strain hardening) (Fig 10d)	0.6789	0.873	0.8927	0.8596	0.838	0.9805

Across 300-500 °C, the LW model attains a high R^2 when A is fit independently for each temperature (exceeding JC at five of six temperatures) but provides more limited accuracy if a constant value of A is used. The original Lin-Wagoner underperforms with an overall mean R^2 of 0.763, although it happens to be the best at 400 °C and 425 °C. The linear $A(T)$ version is strong near the middle of the range, best at 350 °C but drops sharply at 500 °C. The power law model exhibits the lowest mean R^2 value at approximately 0.84 for 300 °C and within the range of 0.63-0.65 by 450-500 °C. This degradation with temperature reflects the model's lack of explicit thermal sensitivity, which is why it trails JC and the modified LW forms. The variant of the modified LW model with no strain hardening term exhibits similar improved response over JC, power law, and unmodified LW, and is the top performer at 500 °C. Overall, Table 2 confirms that a modification to the Lin-Wagoner form to give linear temperature dependence to the yield stress results in more reliable constitutive behavior predictions for AA2618 in the high-

temperature regime than the Johnson-Cook, Lin-Wagoner (unmodified), or power law models.

5. Conclusions

This research investigated the deformation behavior and microstructural evolution of AA2618 under various hot working conditions through a combination of experimental analyses and constitutive modeling. The alloy was studied across temperatures ranging from 300 °C to 500 °C, strain rates of 0.001 s^{-1} and 1.0 s^{-1}, as well as conditions involving abrupt changes in strain rate (strain rate jumps). From these experiments and analyses, the following conclusions about the deformation mechanisms, phase stability, and parameterization of constitutive models were reached:

- For deformation within the temperature range of 300-500 °C, no substantial change in deformation mechanism occurs over four orders of magnitude of strain rate, from 0.001 to 1/s, such that similar microstructures result from deformation under this wide range conditions.
- Flow stresses are highly temperature and strain rate dependent and virtually strain independent in the range of 300-500 °C and 0.001 to 0.1/s, such that most common constitutive models cannot accurately capture the behavior. A modification of the Lin-Wagoner constitutive model to introduce a yield strength that is linearly dependent on temperature results in good reproduction of flow stress behavior. The modified model takes the form

$$\sigma = (A_0 + A_1 T)\{1 - B\exp\big(C_1 + C_2(T - T_0)\big)\varepsilon\}\left(\frac{\dot{\varepsilon}}{\dot{\varepsilon}_0}\right)^m \left(\frac{T}{T_0}\right)^\beta$$

Or, in the case of perfectly plastic behavior with no strain hardening,

$$\sigma = A(T)\left(\frac{\dot{\varepsilon}}{\dot{\varepsilon}_0}\right)^m \left(\frac{T}{T_0}\right)^\beta$$

- Quantitative grain size and shape analyses show that the constitutive behavior can be rationalized by the occurrence of a high rate of dynamic recovery, a modest amount of continuous dynamic recrystallization, and the Zener pinning effects of a stable population of multiple intermetallic phases in this temperature range.

Acknowledgements

The authors are grateful to Queen City Forging Co. for providing the material used in this work and the Forging Industry Educational and Research Foundation (FIERF) for partially funding the research (microgrant award titled “Assessing deviations from flow stress models at the extremes of the aluminum forging range”). The authors wish to thank Prof. A. E. Paz y Puente and Prof. D. Erdeniz for granting access to their laboratory facilities, which were essential for the execution of the experimental work, M. Fickenscher for assistance in the portion of the work performed at the UC Advanced Materials Characterization Center (AMCC), as well as V. Y. Guthula, A. A. Oladipo and N. A. Simpson for their assistance with measurements and helpful discussions.

References

[1] M. Bartošák, I. Šulák, J. Horváth, M. Jambor, L. Pilsová, Isothermal low-cycle fatigue and fatigue–creep behaviour of 2618 aluminium alloy, Int. J. Fatigue 179 (2024) 108027. https://doi.org/10.1016/j.ijfatigue.2023.108027.

[2] F. Nový, M. Janeček, R. Král, Microstructure changes in a 2618 aluminium alloy during ageing and creep, J. Alloys Compd. 487 (2009) 146–151. https://doi.org/10.1016/j.jallcom.2009.08.014.

[3] S. Liu, Q. Pan, M. Li, X. Wang, X. He, X. Li, Z. Peng, J. Lai, Microstructure evolution and physical-based diffusion constitutive analysis of Al-Mg-Si alloy during hot deformation, Mater. Des. 184 (2019) 108181. https://doi.org/10.1016/j.matdes.2019.108181.

[4] H. Wang, G. Qin, C. Li, A modified Arrhenius constitutive model of 2219-O aluminum alloy based on hot compression with simulation verification, J. Mater. Res. Technol. 19 (2022) 3302–3320. https://doi.org/10.1016/j.jmrt.2022.06.080.

[5] Y.C. Lin, Y.-C. Xia, X.-M. Chen, M.-S. Chen, Constitutive descriptions for hot compressed 2124-T851 aluminum alloy over a wide range of temperature and strain rate, Comput. Mater. Sci. 50 (2010) 227–233. https://doi.org/10.1016/j.commatsci.2010.08.003.

[6] B. Wu, M.Q. Li, D.W. Ma, The flow behavior and constitutive equations in isothermal compression of 7050 aluminum alloy, Mater. Sci. Eng. A 542 (2012) 79–87. https://doi.org/10.1016/j.msea.2012.02.035.

[7] X. Peng, X. Zhang, J. Fan, B. Chen, Effect of heating-rate on the thermomechanical behavior of aluminum alloy LY12 and a phenomenological description, Int. J. Solids Struct. 43 (2006) 3527–3541. https://doi.org/10.1016/j.ijsolstr.2005.10.002.

[8] D. Sánchez-Ávila, A. Orozco-Caballero, E. Martínez, L. Portolés, R. Barea, F. Carreño, High-accuracy compliance correction for nonlinear mechanical testing: Improving Small Punch Test characterization, Nucl. Mater. Energy 26 (2021) 100914. https://doi.org/10.1016/j.nme.2021.100914.

[9] Y. Zhang, J.C. Outeiro, T. Mabrouki, On the Selection of Johnson-cook Constitutive Model Parameters for Ti-6Al-4V Using Three Types of Numerical Models of Orthogonal Cutting, Procedia CIRP 31 (2015) 112–117. https://doi.org/10.1016/j.procir.2015.03.052.

[10] J.H. Sung, J.H. Kim, R.H. Wagoner, A plastic constitutive equation incorporating strain, strain-rate, and temperature, Int. J. Plast. 26 (2010) 1746–1771. https://doi.org/10.1016/j.ijplas.2010.02.005.

[11] Z.R. Liu, J.H. Chen, S.B. Wang, D.W. Yuan, M.J. Yin, C.L. Wu, The structure and the properties of S-phase in AlCuMg alloys, Acta Mater. 59 (2011) 7396–7405. https://doi.org/10.1016/j.actamat.2011.08.009.

[12] K. Huang, K. Marthinsen, Q. Zhao, R.E. Logé, The double-edge effect of second-phase particles on the recrystallization behaviour and associated mechanical

properties of metallic materials, Prog. Mater. Sci. 92 (2018) 284–359. https://doi.org/10.1016/j.pmatsci.2017.10.004.

[13] R. Kaibyshev, S. Malopheyev, Mechanisms of Dynamic Recrystallization in Aluminum Alloys, Mater. Sci. Forum 794–796 (2014) 784–789. https://doi.org/10.4028/www.scientific.net/MSF.794-796.784.

[14] H. Mirzadeh, A. Najafizadeh, Flow stress prediction at hot working conditions, Mater. Sci. Eng. A 527 (2010) 1160–1164. https://doi.org/10.1016/j.msea.2009.09.060.

[15] Y. Noh, M.-S. Lee, U.M. Chaudry, T.-S. Jun, Effect of strain rate on the deformation of 6061-T6 aluminum alloy at cryogenic temperature, Mater. Charact. 206 (2023) 113403. https://doi.org/10.1016/j.matchar.2023.113403.

[16] Q. Yang, T. Wojcik, E. Kozeschnik, Continuous Dynamic Recrystallization and Deformation Behavior of an AA1050 Aluminum Alloy during High-Temperature Compression, Metals 14 (2024) 889. https://doi.org/10.3390/met14080889.

[17] E.I. Poliak, J.J. Jonas, A one-parameter approach to determining the critical conditions for the initiation of dynamic recrystallization, Acta Mater. 44 (1996) 127–136. https://doi.org/10.1016/1359-6454(95)00146-7.